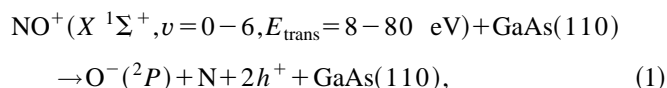


the model. A new procedure for propagating under an asymmetric (non-Hermitian) Hamiltonian is then derived. Finally, the potential energy functions are introduced and the methodology for performing a mixed classical-quantum wave packet calculation is reviewed. In Sec. V, numerical results on the $\text{NO}^+/\text{GaAs}(110)$ system are provided, which are in excellent agreement with experiment. A detailed analysis of the scattering dynamics is provided. Section VI summarizes our main findings.

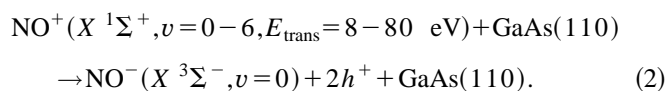
II. EXPERIMENTAL OBSERVATIONS

A number of ion surface scattering experiments have been performed to study the effect of collision energy on the dissociation and electron transfer probabilities at the vacuum/surface interface. Neutralization and electron attachment proceed via resonant and Auger electron transfer,⁹ and molecular ions often demonstrate high threshold energies for dissociation. As for the role of initial vibrational energy in the ion, only the study by Martin *et al.* has directly measured the effect of vibrational excitation on reaction probability.²

The following surface reactions are explored in Ref. 2:



and



Here h^+ represents a hole created in the valence band of GaAs. A state-to-state approach permits incident translational and vibrational energies to be systematically and independently varied, while only the products formed in a particular electronic (vibronic) state are detected.

The survival probability of NO^+ near the GaAs surface was measured to be less than 10^{-6} at 45 eV. This indicates that the first electron transfer is extremely efficient in this system. The second electron transferred from GaAs(110) attaches to molecular or dissociating NO to form NO^- and O^- .

To study the effect of NO^+ translational and vibrational motion on NO^- and O^- formation, two sets of experiments were carried out. (i) NO^+ ($v=1$) ions were scattered at normal incidence on GaAs(110) across a series of collision energies from 10 to 80 eV; (ii) at a fixed collision energy of 45 eV, the initial number of vibrational quanta in incident NO^+ was varied from $v=0$ to 6. The product yield and the translational energy distribution of nascent NO^- ($^3\Sigma^-, v=0$) and O^- (2P) were detected. The relative O^- yield as a function of incident energy is shown in Fig. 1.

Although Eq. (1) is only 4.7 eV endoergic, the observed collision energy threshold occurs at 25 eV. On the other hand, as the vibrational energy is increased from $v=0$ to $v=6$, corresponding to 1.7 eV of vibrational energy, the O^- yield increases by 140%. The same amount of energy in the translational coordinate increases the yield only by 14%. This suggests that vibrational energy is 10 times more efficient than translational energy in producing O^- scattered products. In contrast, it is found that vibrational energy does

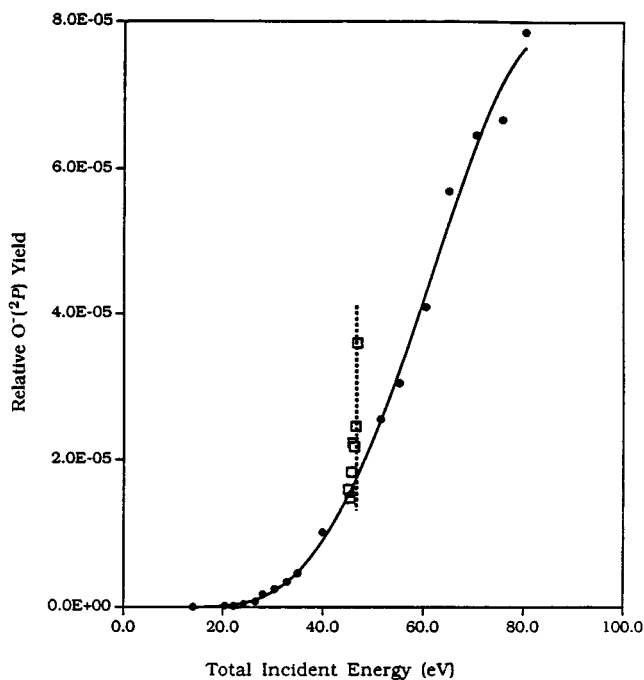


FIG. 1. Experimental relative yield of scattered O^- ions as a function of initial vibrational energy (squares) and translational energy (circles) in NO^+ .

not have a dramatic effect on the NO^- ($^3\Sigma^-, v=0$) yield. The primary goal of this paper is to understand the unique origin of these vibrational dynamics.

III. QUALITATIVE THEORETICAL CONSIDERATIONS

This section briefly reviews the existing theoretical framework relevant to the aforementioned experimental system. The important processes involved in Eqs. (1) and (2) are energy transfer between translation, molecular vibration, rotation, and surface phonons; and electron transfer between the molecule and the surface resulting in nonadiabatic nuclear dynamics for the molecule. In the following sections, we will categorize the initial conditions as being either energetic or geometric in nature.

A. Energetics

1. Electron transfer process

Associated with Eqs. (1) and (2) is the transfer of two electrons from GaAs. Neutralization of NO^+ and electron attachment to NO have been discussed in detail by Jacobs and co-workers.² Resonant electron transfer can occur when an energy state of the neutral molecule is degenerate with a filled state at the surface. Due to the paucity of NO electronic states degenerate with the GaAs(110) density of states, only the ground $X^2\Pi$ state of NO is likely to be filled via neutralization.

Neutralization of atoms and molecules near surfaces has been modeled quantum mechanically by several authors. One notable approach developed by Anderson¹⁰ and Newns,¹¹ and reviewed by Los and Geerlings¹² treats a localized atomic state coupled to a continuum of bulk states. The one electron Hamiltonian can be written as

$$H(z) = \sum_k \epsilon_k n_k + \epsilon_a(z) n_a + \sum_k [V_{ak}(z) c_a^\dagger c_k + V_{ak}^*(z) c_k^\dagger c_a]. \quad (3)$$

Here n is the number operator, ϵ is the energy of the wave function, c^\dagger and c are creation and annihilation operator, z is the atom–surface distance, and V_{ak} is the transition matrix element connecting the atomic and surface states. The level width of the atomic state is approximated by Fermi's Golden Rule,

$$\Delta = 2\pi \sum_k \rho(\epsilon_a) |V_{ak}|^2, \quad (4)$$

where $\rho(\epsilon_a)$ is the density of atomic states at energy ϵ_a . Assuming that $z = z(t)$ (i.e., the z -dependence is replaced by t) and that the k and t dependence of $V_{ak}(t)$ are separable, we have

$$V_{ak}(z) = V_{ak}(t) = V_{ak} u(t), \quad (5)$$

where $u(t)$ takes into account all the z -dependence of the coupling potential. In this case, Eq. (20) of Ref. 12 can be solved analytically,

$$\begin{aligned} \langle n_a(t) \rangle &= \langle n_a(-\infty) \rangle e^{-\int_{-\infty}^t \Delta(t') dt'} + \pi^{-1} \int d\epsilon f(\epsilon, T) \\ &\times \left| \int_{-\infty}^t \left[\frac{1}{2} \Delta(t') \right]^{1/2} \right. \\ &\times \left. e^{-i\epsilon t' - \int_{t'}^t [i\epsilon_a(t'') + 1/2\Delta(t'')] dt''} dt' \right|^2, \quad (6) \end{aligned}$$

where $f(\epsilon, T)$ is the Fermi distribution as a function of energy and temperature.

Equation (6) provides a point of comparison for the proposed electron transfer model. Both resonant and Auger electron transfer can mediate neutralization.⁹ The characteristic length scale for these tunneling processes confines neutralization to occur within a few angstroms of the surface. Electron attachment to NO proceeds only through resonant transfer, populating the $X^3\Sigma^-$ ground state of NO^- . Electron transfer has been implicated in the dissociation of many molecules at surfaces.¹³ However, in the present system, a vertical transition from $\text{NO}^+(v^+)$ to $\text{NO}^-(v^-)$ alone delivers an insufficient amount of energy to dissociate NO^- .

2. Energy redistribution

The collision energy is redistributed into electron–hole pairs, surface phonons, product translation, product vibration, and product rotation. The experimental threshold for O^- emergence is observed at 25 eV, which is much higher than the dissociation energy for either NO (6.56 eV) or NO^- (4.6 eV). Only 6% of the $\text{NO}^+(X^1\Sigma^+, v^+=1)$ incident energy is retained as $\text{NO}^-(X^3\Sigma^-, v^-=0)$ translational energy; similarly, O^- scatters with only 13% of the incident energy. These experimental observations strongly suggest that CID is a major contributor to molecular dissociation in this system.²

The CID mechanism attributes dissociation to an impulsive transfer of incident translational energy into rovibrational energy. Classical trajectory calculations involving a rotating, vibrating NO diatom colliding with a single surface atom have been applied to the NO/GaAs system.¹⁴ These

calculations proceeded on a single diabatic potential energy surface so as to isolate the role of impulsive energy transfer in the dissociation dynamics. These studies demonstrate that the collision energy transfer depends on the incident translational energy, the initial NO^+ vibrational quanta, the phase of molecular vibration prior to impact, the alignment of the internuclear axis relative to the surface normal, and the surface impact site.^{14–16}

The CTC model accurately predicts the O^- threshold and suggests that the predominant part of the initial translational energy (70%–80%) is transferred to surface vibrational motion. However, the CTC model fails to reproduce the observed correlation between initial vibrational energy and dissociation probability. Nevertheless, it should be noted that the dissociation probability is sensitive to the phase of molecular vibration. The model predicts that molecules with a compressed phase near the surface may be twice as likely to dissociate as those colliding with a stretched phase.

Rotational excitation upon impact can also mediate CID. Centrifugal forces couple nascent rotational energy to a vibrational stretching motion in the diatom. The centrifugal mechanism was implicated in the dissociative scattering of I_2 on MgO(100) (Ref. 17) and of O_2 on Ag(111).¹⁸ These results underscore the importance of rotational excitation in the CID mechanism.

B. Approach geometry

The relative contribution of direct vibrational excitation vs rotational excitation in CID depends strongly on the approach geometry of the incident molecule. A CTC study simulating the scattering of aligned NO^+ on Ag(111) has highlighted three distinct scattering regimes; head-on collision, centrifugal recoil, and chattering. In head-on collisions, the transfer of incident translational energy to vibrational motion reaches a maximum within 10 fs; however, much of the energy transfers back into the translational coordinate as the molecule recoils away from surface. In fact, for a pure head-on collision the net energy transfer from translation to vibration is negligible. For approach geometries where the molecular axis lies off the surface normal, the molecule is more likely to dissociate, because the collision induces a torque on the molecule. Molecular reorientation upon impact reduces the degree to which vibrational energy will be transferred back into translational energy during recoil. Moreover, rotational excitation itself promotes dissociation through a centrifugal force. Figure 2 illustrates a molecule colliding with a surface atom; momentum transfer gives an impulsive “kick,” resulting in vibrational compression and rotational excitation; dissociation ensues as the molecule recoils, and rotational energy is eventually converted to vibrational energy. For incident orientations where the molecular axis lies closer to the surface plane, rotational excitation dominates the energy transfer process. However, chattering can greatly reduce the net rotational excitation if a second collision by the other end of the molecule occurs. Consequently, dissociation is quenched in the chattering regime. Overall, the approach geometry of the molecule dictates the energy redistribution in the scattering process.

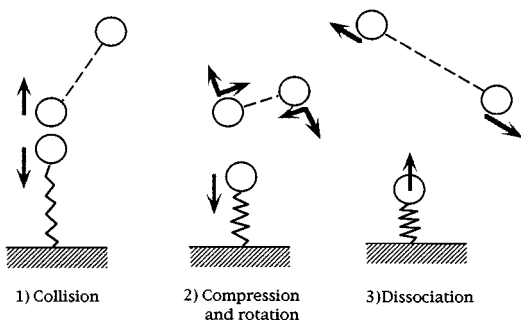


FIG. 2. A sketch of the collision induced dissociation (CID) mechanism.

C. Interplay between electron transfer and energy transfer processes

Many atomic ion scattering experiments suggest that a system loses memory of its initial electronic state following a collision with the surface.¹² However, in molecules, there can still be memory of the initial vibrational state, even when electron transfer is operative.² Because motion along the vibrational coordinate differs within each electronic state, the evolution of intramolecular motion depends on the exact sequence of electronic transitions.

In this study, the incoming molecules are prepared in a specific vibrational eigenstate of the ground electronic state of NO^+ . As NO^+ ions approach the GaAs surface, an electron can tunnel from the surface to the molecule. Based on the Franck–Condon principle, the molecule maintains its former nuclear configuration during the rapid electronic transition. Since the equilibrium bond length of NO^+ is shorter than that of NO , the NO^+ wave function will be vertically projected onto the repulsive region of the NO PES forming a coherent vibrational wave packet. The neutral molecule subsequently collides with the surface and undergoes vibrational compression along with rotational excitation. Because the interaction time (typically 15 fs) is comparable to the period of vibrational motion (typically ≥ 20 fs), the vibrational wave packet will not dephase dramatically between neutralization and impact. As the wave packet continues to evolve on the neutral NO PES, the portion representing energies higher than the dissociation energy of NO will dissociate into N and O . Concurrently, a transition to the NO^- PES may give rise to either NO^- or N and O^- products. Electron attachment to NO is most probable for large internuclear separations, peaking at 1.7 Å. It should be noted that the experimental results suggest that the final O^- fragment originates from CID of NO rather than NO^- .²

D. Simulation of the vibrational coherence via wave packet methods

The above discussion provides strong motivation for pursuing wave packet methods to simulate the vibrational coherence. We outline the considerations as follows:

- (i) The coherent vibrational effect is a wave effect and only a quantum mechanical description is fully accurate. Furthermore, electron transfer is intrinsically a nonadiabatic process, whereas classical trajectory cal-

culations are only valid on a single PES. Although more sophisticated methods such as surface hopping can be applied to treat the electronic transfer process,¹⁹ an exact quantum calculation is still preferable when it is tractable.

- (ii) By using a time-dependent self-consistent field (TD-SCF) treatment we can treat the primary degrees of freedom fully quantum mechanically and the secondary degrees of freedom, such as rotation and surface atom motion classically.
- (iii) In a time-dependent calculation, we can monitor the probability amplitudes in each channel through time and thus follow the real time dynamics of the scattering. This is very important in understanding the interplay between electron transfer and energy transfer. At hyperthermal collision energies, the interaction duration is subpicosecond, and a time-dependent wave packet calculation is a more natural way to obtain a physical interpretation and visualization of the process than a time-independent calculation.

Overall, a wave packet calculation instead of a density matrix calculation²⁰ will be sufficient to obtain all of the necessary information with maximum efficiency.

IV. BUILDING BLOCKS

The simulation presented in this paper uses a time-dependent self-consistent field (TDSCF) approach. It treats the electron transfer process and translational and vibrational motion quantum mechanically, while treating other degrees of freedom classically. In addition to a classical treatment of molecular rotation and surface vibration, we make several other standard approximations.

- (1) Born–Oppenheimer separation of electronic and nuclear degrees of freedom.
- (2) Empirical potential energy surfaces for ground and excited states of the intramolecular and intermolecular interactions and empirical coupling matrix elements. For simplicity, the latter are taken to be independent of molecular orientation and separation.
- (3) Interaction with only a single surface atom. A hyperthermal energy collision involves predominantly a short range repulsive interaction between the molecule and the single closest surface atom. Although an incident molecule may undergo multiple collisions with the corrugated GaAs(110) surface, it is believed that the initial collision is primarily responsible for the dissociation dynamics.¹⁵

In the following sections, our methodology is described in detail. We begin with a derivation of the reduced effective Hamiltonian matrix for electron transfer. Then we turn to the TDSCF equations and wave packet propagation methods used to describe the energy transfer process.

A. Multisurface crossing

Quantum mechanical calculations of nonadiabatic processes, such as electron transfer, internal conversion, and intersystem crossing, have been studied extensively in the gas

phase.²¹ However, the literature on electron transfer processes at surfaces is much more limited. Previous models have described surface electron transfer as a coupling between two diabatic surfaces. For example, for both gas phase molecules and chemisorbed molecules the Schrodinger equation for the wave functions can be written as

$$i\hbar \frac{\partial}{\partial t} \begin{pmatrix} \psi_1 \\ \psi_2 \end{pmatrix} = \begin{pmatrix} H_1 & V_{12} \\ V_{21} & H_2 \end{pmatrix} \begin{pmatrix} \psi_1 \\ \psi_2 \end{pmatrix}. \quad (7)$$

Here the subscripts 1 and 2 denote the electronic state, and $V_{12}(V_{21})$ represents the coupling between these two states. However, a simple curve-crossing picture is not valid for the case where a primary electronic state is coupled to a *band* of surface states. As discussed in Sec. III A 1, neutralization forms a hole, h^+ , somewhere in the surface valence band in conjunction with the $\text{NO } X^2\Pi$ state. Thus, the $\text{NO}^+ X^1\Sigma^+$ state will couple with a band of $(\text{NO } X^2\Pi + h_i^+)$ states that are displaced by infinitesimal energy shifts. It is possible to approximate this process by finite quadrature as a coupling of a primary state to a finite group of states, as shown in Fig. 3. The index i denotes the energy level of h_i^+ , where $i=1$ represents the Fermi level and $i=n$ represents the valence band minimum. Similar models have been discussed by Bauer *et al.*²² and Gadzuk,²³ where they modeled the atom-

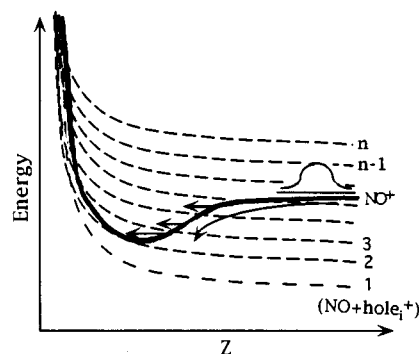


FIG. 3. A sketch of coupling between the NO^+ -GaAs potential energy curve and the band of $(\text{NO}^+ + h^+)$ -GaAs potential energy curves. The h^+ can originate across a continuum within the valence band.

molecule interaction as a curve crossing with a manifold of curves. The coupling between the $(\text{NO } X^2\Pi + h_i^+)$ state and the $(\text{NO}^- X^3\Sigma^- + h_i^+ + h_1^+)$ state further complicates the process, but conveniently, due to energetic restrictions, electron attachment to form NO^- involves predominantly the transfer of an electron from the Fermi level. Thus each neutral $(\text{NO } X^2\Pi + h_i^+)$ state will couple simply to a single $(\text{NO}^- X^3\Sigma^- + h_i^+ + h_1^+)$ state. The Hamiltonian can be written as

$$H\Psi = \begin{pmatrix} H_{\text{NO}^+} & V_{a1} & V_{a2} & \cdots & V_{an} & 0 & 0 & \cdots & 0 \\ V_{1a} & H_{\text{NO},1} & 0 & \cdots & 0 & V_{b1} & 0 & \cdots & 0 \\ V_{2a} & 0 & H_{\text{NO},2} & \cdots & 0 & 0 & V_{b2} & \cdots & 0 \\ \vdots & \vdots & \vdots & \ddots & \vdots & \vdots & \vdots & \vdots & \vdots \\ V_{na} & 0 & 0 & \cdots & H_{\text{NO},n} & 0 & 0 & \cdots & V_{bn} \\ 0 & V_{1b} & 0 & \cdots & 0 & H_{\text{NO}^-,1} & 0 & \cdots & 0 \\ 0 & 0 & V_{2b} & \cdots & 0 & 0 & H_{\text{NO}^-,2} & \cdots & 0 \\ \vdots & \vdots & \vdots & \vdots & \vdots & \vdots & \vdots & \ddots & \vdots \\ 0 & 0 & 0 & \cdots & V_{nb} & 0 & 0 & \cdots & H_{\text{NO}^-,n} \end{pmatrix} \begin{pmatrix} \psi_{\text{NO}^+} \\ \psi_{\text{NO},1} \\ \psi_{\text{NO},2} \\ \vdots \\ \psi_{\text{NO},n} \\ \psi_{\text{NO}^-,1} \\ \psi_{\text{NO}^-,2} \\ \vdots \\ \psi_{\text{NO}^-,n} \end{pmatrix}. \quad (8)$$

We can rewrite these equations as a set of time-dependent Schrödinger equations,

$$i\hbar \frac{\partial}{\partial t} |\psi_{\text{NO}^+}\rangle = H_{\text{NO}^+} |\psi_{\text{NO}^+}\rangle + \sum_i^n (V_{ai} |\psi_{\text{NO},i}\rangle), \quad (9a)$$

$$i\hbar \frac{\partial}{\partial t} |\psi_{\text{NO},i}\rangle = V_{ia} |\psi_{\text{NO}^+}\rangle + H_{\text{NO},i} |\psi_{\text{NO},i}\rangle + V_{bi} |\psi_{\text{NO}^-,i}\rangle \quad (i=1, n), \quad (9b)$$

$$i\hbar \frac{\partial}{\partial t} |\psi_{\text{NO}^-,i}\rangle = V_{ib} |\psi_{\text{NO},i}\rangle + H_{\text{NO}^-,i} |\psi_{\text{NO}^-,i}\rangle \quad (i=1, n). \quad (9c)$$

In order to reduce the space of the dynamics, we sum over the n equations in Eqs. (9b) and (9c) to obtain

$$i\hbar \frac{\partial}{\partial t} \sum_i^n (|\psi_{\text{NO},i}\rangle) = \left(\sum_i^n V_{ia} \right) |\psi_{\text{NO}^+}\rangle + \sum_i^n (H_{\text{NO},i} |\psi_{\text{NO},i}\rangle) + \sum_i^n (V_{bi} |\psi_{\text{NO}^-,i}\rangle), \quad (9d)$$

$$i\hbar \frac{\partial}{\partial t} \sum_i^n (|\psi_{\text{NO}^-,i}\rangle) = \sum_i^n (V_{ib} |\psi_{\text{NO},i}\rangle) + \sum_i^n (H_{\text{NO}^-,i} |\psi_{\text{NO}^-,i}\rangle). \quad (9e)$$

Note that the surface states are displaced by small energies. Thus, we can write

$$H_{\text{NO},i} = H_{\text{NO}} + A_i, \quad (10a)$$

$$H_{\text{NO}^-,i} = H_{\text{NO}^-} + B_i. \quad (10b)$$

Also, we assume the nondiabatic coupling function is real and is independent of index i ,

$$V_{ai} = V_{ia} = V_a, \quad (11a)$$

$$V_{bi} = V_{ib} = V_b. \quad (11b)$$

Thus Eqs. (9a)–(9e) can be simplified as follows:

$$i\hbar \frac{\partial}{\partial t} |\psi_{\text{NO}^+}\rangle = H_{\text{NO}^+} |\psi_{\text{NO}^+}\rangle + V_a \sum_i^n |\psi_{\text{NO},i}\rangle, \quad (12a)$$

$$\begin{aligned} i\hbar \frac{\partial}{\partial t} \sum_i^n (|\psi_{\text{NO},i}\rangle) \\ = nV_a |\psi_{\text{NO}^+}\rangle + H_{\text{NO}} \sum_i^n |\psi_{\text{NO},i}\rangle + \sum_i^n (A_i |\psi_{\text{NO},i}\rangle) \\ + V_b \sum_i^n |\psi_{\text{NO}^-,i}\rangle, \end{aligned} \quad (12b)$$

$$\begin{aligned} i\hbar \frac{\partial}{\partial t} \sum_i^n (|\psi_{\text{NO}^-,i}\rangle) \\ = V_b \sum_i^n |\psi_{\text{NO},i}\rangle + H_{\text{NO}^-} \sum_i^n |\psi_{\text{NO}^-,i}\rangle \\ + \sum_i^n (B_i |\psi_{\text{NO}^-,i}\rangle). \end{aligned} \quad (12c)$$

Let

$$|\psi_{\text{NO}}\rangle = \sum_i^n (|\psi_{\text{NO},i}\rangle), \quad (13a)$$

$$|\psi_{\text{NO}^-}\rangle = \sum_i^n (|\psi_{\text{NO}^-,i}\rangle), \quad (13b)$$

$$A(x,t) = \frac{\sum_i^n (A_i |\psi_{\text{NO},i}\rangle)}{\sum_i^n |\psi_{\text{NO},i}\rangle}, \quad (13c)$$

and

$$B(x,t) = \frac{\sum_i^n (B_i |\psi_{\text{NO}^-,i}\rangle)}{\sum_i^n |\psi_{\text{NO}^-,i}\rangle}. \quad (13d)$$

We thus have

$$i\hbar \frac{\partial}{\partial t} |\psi_{\text{NO}^+}\rangle = H_{\text{NO}^+} |\psi_{\text{NO}^+}\rangle + V_a |\psi_{\text{NO}}\rangle, \quad (14a)$$

$$\begin{aligned} i\hbar \frac{\partial}{\partial t} |\psi_{\text{NO}}\rangle = nV_a |\psi_{\text{NO}^+}\rangle + [H_{\text{NO}} + A(x,t)] |\psi_{\text{NO}}\rangle \\ + V_b |\psi_{\text{NO}^-}\rangle, \end{aligned} \quad (14b)$$

$$i\hbar \frac{\partial}{\partial t} |\psi_{\text{NO}^-}\rangle = V_b |\psi_{\text{NO}}\rangle + [H_{\text{NO}^-} + B(x,t)] |\psi_{\text{NO}^-}\rangle. \quad (14c)$$

Thus, this primary state/band of states coupling can be simulated by a simple asymmetric time-dependent Hamiltonian. This asymmetric structure of the Hamiltonian is essential to describe the virtually complete and irreversible nature of the neutralization step, $\text{NO}^+ \rightarrow \text{NO}$ in a reduced space. Any Hermitian form for the Hamiltonian would lead to significant back transfer of amplitude from NO to NO^+ . Note, however, that the price for using an asymmetric Hamiltonian is that the total normalization of the wave functions $\|\psi_{\text{NO}^+}\| + \|\psi_{\text{NO}}\| + \|\psi_{\text{NO}^-}\|$ will not be strictly conserved. In the next section a transformation is described which circumvents this problem.

B. Propagation under an asymmetric Hamiltonian

In this section we will derive a novel method to transform the propagation of an asymmetric Hamiltonian into that of a symmetric one. From Eq. (14), we have

$$\begin{aligned} i\hbar \frac{\partial}{\partial t} \begin{pmatrix} \psi_{\text{NO}^+} \\ \psi_{\text{NO}} \\ \psi_{\text{NO}^-} \end{pmatrix} \\ = \begin{pmatrix} H_{\text{NO}^+} & V_a & 0 \\ nV_a & H_{\text{NO}^+} + A(t) & V_b \\ 0 & V_b & H_{\text{NO}^-} + B(t) \end{pmatrix} \begin{pmatrix} \psi_{\text{NO}^+} \\ \psi_{\text{NO}} \\ \psi_{\text{NO}^-} \end{pmatrix}. \end{aligned} \quad (15)$$

Let

$$\begin{aligned} |\psi_{\text{NO}^+}(t)\rangle &= \epsilon_1(t) |\phi_{\text{NO}^+}\rangle, \\ |\psi_{\text{NO}}(t)\rangle &= \epsilon_2(t) |\phi_{\text{NO}}\rangle, \\ |\psi_{\text{NO}^-}(t)\rangle &= \epsilon_3(t) |\phi_{\text{NO}^-}\rangle. \end{aligned} \quad (16)$$

Substituting Eq. (16) into Eq. (15), we have

$$i\hbar \frac{\partial}{\partial t} \begin{pmatrix} \phi_{\text{NO}^+} \\ \phi_{\text{NO}} \\ \phi_{\text{NO}^-} \end{pmatrix} = \begin{pmatrix} H_{\text{NO}^+} - i\hbar \frac{\partial \ln \epsilon_1}{\partial t} & \frac{\epsilon_2}{\epsilon_1} V_a & 0 \\ n \frac{\epsilon_1}{\epsilon_2} V_a & H_{\text{NO}^+} + A(t) - i\hbar \frac{\partial \ln \epsilon_2}{\partial t} & \frac{\epsilon_3}{\epsilon_2} V_b \\ 0 & \frac{\epsilon_2}{\epsilon_3} V_b & H_{\text{NO}^-} + B(t) - i\hbar \frac{\partial \ln \epsilon_3}{\partial t} \end{pmatrix} \begin{pmatrix} \phi_{\text{NO}^+} \\ \phi_{\text{NO}} \\ \phi_{\text{NO}^-} \end{pmatrix}. \quad (17)$$

Whether or not the total normalization of the wave functions $\|\phi_{\text{NO}^+}\| + \|\phi_{\text{NO}}\| + \|\phi_{\text{NO}^-}\|$ is conserved depends on the choice of $\epsilon_1(t)$ and $\epsilon_2(t)$. In order to construct a norm-conserving symmetric Hamiltonian, we set

$$\sqrt{n}\epsilon_1(t) = \epsilon_2(t) = \epsilon_3(t) = \text{constant}. \quad (18)$$

Now we have a symmetric Hamiltonian,

$$i\hbar \frac{\partial}{\partial t} \begin{pmatrix} \phi_{\text{NO}^+} \\ \phi_{\text{NO}} \\ \phi_{\text{NO}^-} \end{pmatrix} = \begin{pmatrix} H_{\text{NO}^+} & \sqrt{n}V_a & 0 \\ \sqrt{n}V_a & H_{\text{NO}^+} + A(t) & V_b \\ 0 & V_b & H_{\text{NO}^-} + B(t) \end{pmatrix} \begin{pmatrix} \phi_{\text{NO}^+} \\ \phi_{\text{NO}} \\ \phi_{\text{NO}^-} \end{pmatrix}. \quad (19)$$

It is simple to recover the original observables from the new variables. For example, to evaluate the survival probability of NO^+ ,

$$P_{\text{NO}^+} = \frac{|\psi_{\text{NO}^+}|^2}{|\psi_{\text{NO}^+}|^2 + |\psi_{\text{NO}}|^2 + |\psi_{\text{NO}^-}|^2} = \frac{|\phi_{\text{NO}^+}|^2}{|\phi_{\text{NO}^+}|^2 + n(|\phi_{\text{NO}}|^2 + |\phi_{\text{NO}^-}|^2)}. \quad (20)$$

C. Reduced dimensional model

Although surface reactions involve multidimensional potential energy hypersurfaces, a reduced-dimensionality treatment is needed to make the problem numerically tractable. We use the conventional coordinates for the diatomic molecule/surface system, as shown in Fig. 4. The coordinates consist of Z (normal distance between the molecule's center-of-mass and the surface), r (the diatom's internuclear separation), θ (the orientation of the molecule's internuclear axis relative to the surface normal), and Z_1 (the surface atom's displacement from equilibrium). It is assumed that the surface reaction is identical for different azimuthal angles of the molecule, thus this coordinate is neglected. Also for simplicity the corrugation of the surface is neglected, and thus out-of-plane motion of the molecule is eliminated from the calculation. Surface motion is incorporated by connecting the surface atom to an infinite-mass substrate through a simple harmonic oscillator (SHO).²⁴ It is discussed in Ref. 14 that the SHO model is valid, because at hyperthermal energies the short range repulsive portion of the PES dominates the interactions; moreover, as a result of the short collision time (around 10–20 fs), the scattered diatom will escape the molecule/surface interaction region before the impacted surface atom's motion can effectively couple to lattice phonons. The Hamiltonian of this system can be written as

$$H_j = -\frac{\hbar^2}{2m_{\text{Ga}}} \frac{\partial^2}{\partial Z_1^2} - \frac{\hbar^2}{2m_{\text{NO}}} \frac{\partial^2}{\partial Z^2} - \frac{\hbar^2}{2\mu} \left(\frac{\partial^2}{\partial r^2} + \frac{1}{r^2} \frac{\partial^2}{\partial \theta^2} \right) + V_j(Z_1, Z, r, \theta), \quad (21)$$

where $j=1,2,3$ corresponds to NO^+ , NO , and NO^- , respectively, and μ is the reduced mass for the NO diatom. The

single surface atom employed in the model is arbitrarily selected to be Ga. Because the masses of Ga and As differ by only 7%, a collision with either surface atom will result in similar energy transfer to the surface.

D. Potential energy surfaces

Three different pairwise additive molecule/surface potentials were used in the CTC calculation by Martin *et al.*:¹⁴ A Born–Mayer potential, a Ziegler–Biersack–Littmark potential, and a Hartree–Fock potential. It was reported there that the three types of PES gave very similar results. Here, we use only the Born–Mayer potential. At hyperthermal collision energies, the gas–surface interaction is predominantly repulsive, and thus a purely repulsive pairwise additive potential combined with Coulombic attraction between the ion and its image charge is a reasonable approximation, ($V_{j,1}$). For the molecular vibrational coordinate, a Morse potential is used for each electronic state, where the Morse parameters are computed from NO^+ , NO , and NO^- spectroscopic measurements, ($V_{j,2}$). As discussed above, the surface atom is described by a simple harmonic oscillator, (V_3). The experimental surface phonon frequency range is from 200 cm^{-1} to 800 cm^{-1} . We choose a moderate value of 300 cm^{-1} , for which the simulations predict that 8% of the incident energy remains in translational energy of the NO^- product. This reproduces the experimental value very well. The overall potential for this system is

$$V_j(Z_1, Z, r, \theta) = V_{j,1}(Z - Z_1) + V_{j,2}(r) + V_3(Z_1), \quad (22a)$$

$$V_{j,1} = C \left\{ e^{-[Z - Z_1 - (\mu r \cos \theta / m_N) / \alpha]} + e^{-[Z - Z_1 + (\mu r \cos \theta / m_O) / \alpha]} \right\} + \frac{(\epsilon - 1) Q_j^2}{4(\epsilon + 1)(Z - Z_1)}, \quad (22b)$$

$$V_{j,2}(r) = D_j [1 - e^{-\gamma_j(r - r_{e,j})}]^2, \quad (22c)$$

and

$$V_3(Z_1) = \frac{1}{2} k_Z Z_1^2, \quad (22d)$$

where $\gamma_j = \omega_j \sqrt{(\mu / 2D_j)}$. The parameters used within the PES are summarized in Table I. In Eq. (22b), Q_j represents

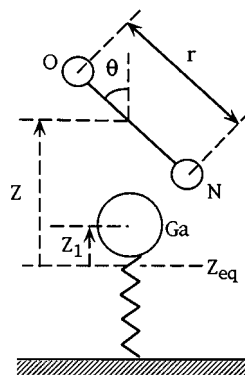


FIG. 4. The coordinate system for a rotating vibrating diatom interacting with a single surface atom.

TABLE I. Parameters used in NO⁺/GaAs reactive scattering.

C	α	1.1 k_z	Δ_0	β
5432 eV	0.2722 Å	0.26 eV/Å ⁻²	13.9 eV	1.2 Å ⁻¹
State	D_j	1.2 ω_j	$r_{e,j}$	
NO ⁺	10.6 eV	2370 cm ⁻¹	0.982 Å	
NO	6.56 eV	1904 cm ⁻¹	1.15 Å	
NO ⁻	5.19 eV	1470 cm ⁻¹	1.26 Å	

the formal charge of the diatom ($Q_j = 2 - j$) and ϵ is taken to be 12, the static dielectric constant for bulk GaAs. The off-diagonal terms V_a and V_b are approximated as exponential functions of Z . This exponential form is motivated by the exponential dependence of the Δ function in the Anderson–Newns equation as will be discussed immediately below.¹²

E. Model parameters

The treatment presented here borrows heavily from the concepts underlying the Anderson–Newns formalism. In the Anderson–Newns approach, the one-electron wave function is represented by a time-dependent superposition of the atomic affinity level and the continuum of metal states. The occupation of the affinity level translates directly into a neutralization probability for the incident atomic ion. In our approach, we treat neutralization as the coupling between the molecular ion state and a dressed state involving the neutral molecule and a nascent hole formed in the valence band. The first two terms in Eq. (3) are analogous to the diagonal matrix elements displayed in the upper left quadrant of the matrix in Eq. (8). Furthermore, the final terms in Eq. (3) couple the one-electron states in a manner similar to the off-diagonal matrix elements in Eq. (8). Therefore, we have adapted Eq. (4) to relate V_a and V_b to the affinity level width, Δ ,

$$V_a = \sqrt{\frac{\Delta}{2\pi n}}, \quad (23a)$$

$$V_b = \sqrt{\frac{\Delta}{2\pi}}. \quad (23b)$$

In Eq. (23a), n is the total number of discrete surface states across the valence band that may couple to the molecular state. The value of n was chosen to give the same rate of neutralization in the simulation as calculated by the Anderson–Newns equation.

Newns¹¹ has noted that the level width or lifetime broadening of an atomic (molecular) state typically exhibits an exponential dependence on Z ,

$$\Delta(Z) = \Delta_0 e^{-\beta Z}. \quad (23c)$$

Here, Δ_0 and β (Table I) are extrapolated from the *ab initio* calculations of Norlander *et al.*²⁵ These parameters demonstrate a characteristic dependence on the atomic (molecular) affinity level.

From the definition of $A(t)$ in Eq. (13c), $A(t) \approx A_i$, where A_i is the energy shift for the state where the amplitude of the wave packet is maximum. Based on the Landau–Zener model, maximal crossing between the two surfaces occurs where the energy difference between the two is smallest. Since the surface electronic band is from -4.7 eV to -12 eV, and the ionization potential of NO is -9.8 eV, NO⁺ always crosses with at least one of the (NO+ h_i^+) states. Thus $A(t)$ is defined so that NO⁺ and (NO+ h_i^+) are always resonant at the center position of the wave packet. As discussed in Sec. IV A, the (NO⁻+ h_i^+ + h_1^+) curve is closest to crossing the (NO+ h_i^+) curve at the valence band maximum. Thus, we take $B(t) = A(t) - 4.7$ eV.

F. Treatment of molecular rotation and surface motion

Multidimensional wave packet calculations can be very demanding computationally. Thus, we employ several approximations in order to reduce the size of our calculation. Mean field approximations such as time-dependent self-consistent field theory (TDSCF) (Ref. 26) are generally used to treat those dimensions that are weakly coupled. The idea of such approaches is to break a multidimensional calculation into several reduced-dimensional calculations, where the equations of motion are coupled through a time-dependent mean field. The transfer of energy between the different coordinates is taken into account such that the total energy is conserved. Standard wave packet techniques can be applied directly to the calculation without extensive modifications. In this approach the classical variables are integrated by Hamilton’s equations of motion. Mixed classical-quantum calculations have been reported by Jackson and co-workers,⁵ Kossloff and Citri,⁸ and many others.

Considering the nature of our system, namely highly impulsive motion in Z , vibrational motion in r , and relatively slower motion in rotation and surface atom vibration, it is reasonable that rotation and surface vibration can be treated as providing a mean field in which the wavepacket propagates along the Z and r coordinates. The rotational motion obeys the following equations:

$$L = I\dot{\theta}, \quad (24a)$$

$$I = \mu\langle r \rangle^2, \quad (24b)$$

$$\dot{L} = - \sum_j \left\langle \frac{\partial V_j}{\partial \theta} \right\rangle P_j, \quad (24c)$$

where I is the molecule’s momentum of inertia and L is the angular momentum, and the population P_j is calculated in the manner of Eq. (20). The surface vibration obeys the following equations:

$$P_{Z_1} = m_{\text{Ga}} \dot{Z}_1, \quad (25a)$$

$$\dot{P}_{Z_1} = - \sum_j \left\langle \frac{\partial V_j}{\partial Z_1} \right\rangle P_j. \quad (25b)$$

Assuming a uniform rotational angular momentum, L , across r and Z , the rotational term in the quantum mechanical Hamiltonian [Eq. (21)] becomes a centrifugal potential term with respect to r , i.e.,

$$-\frac{\hbar^2}{2\mu r^2} \frac{\partial^2}{\partial \theta^2} = \frac{L^2}{2\mu r^2}. \quad (26)$$

G. Wave packet propagation

A two-dimensional wave packet calculation is performed in Z and r . In evaluating the Hamiltonian, the fast Fourier transform (FFT) method²⁷ is used to evaluate the momentum operator, and local multiplication is used to evaluate the potential operator. A short iterative Lanczos algorithm (SIL) (Ref. 28) is utilized to evaluate the evolution operator.

Here a technique of shifting both momentum and coordinate space reduces the number of grid points in the Z coordinate. The ordinary propagation in the Schrödinger representation is given by

$$i\hbar \frac{\partial \Phi_S(t)}{\partial t} = H\Phi_S(t). \quad (27)$$

In order to reduce the number of grid points, a wave function, $\Phi'_S(t)$, is formed by an appropriate shift in the conjugate space. This wave function is given as

$$\Phi'_S(t) = e^{i\Delta Z \hat{P}} e^{-i\Delta P \hat{Z}} \Phi_S(t). \quad (28)$$

Thus

$$\Phi_S(t) = e^{i\Delta P \hat{Z}} e^{i\Delta Z \hat{P}} \Phi'_S(t). \quad (29)$$

Here $\Delta Z = Z(t + \Delta t) - Z(t)$ and $\Delta P = P(t + \Delta t) - P(t)$. The new momentum-shifted wave packet has far fewer oscillations in coordinate space, and thus requires less grid points. Similarly, the coordinate-shifted wave packet also requires far fewer grid points than the unshifted wave packet.

If the total Hamiltonian is written as

$$H = T(P) + V(Z), \quad (30)$$

then

$$\begin{aligned} H\Phi_S(t) &= [T(P) + V(Z)] e^{i\Delta P \hat{Z}} e^{-i\Delta Z \hat{P}} \Phi'_S(t) \\ &= e^{i\Delta P \hat{Z}} e^{-i\Delta Z \hat{P}} [T(P + \Delta P) + V(Z + \Delta Z)] \Phi'_S(t). \end{aligned} \quad (31)$$

Substituting Eq. (31) into Eq. (27) yields

$$i\hbar \frac{\partial \Phi'_S(t)}{\partial t} = [T(P + \Delta P) + V(Z + \Delta Z)] \Phi'_S(t). \quad (32)$$

Therefore motion of the shifted wave function also obeys a Schrödinger-type equation of motion.

H. O⁻ yield and NO⁻ vibrational distribution

The yield of O⁻ dissociated from the NO⁻ PES can be calculated by monitoring the population of the wave function that escapes from the (N–O)⁻ Morse well. An absorbing boundary is applied at $r = 3 \text{ \AA}$ to avoid reflection in the vi-

brational coordinate. The flux operator is calculated right before the absorbing boundary using the following equations:

$$\begin{aligned} \mathbf{F}(Z, t) &= \frac{i\hbar}{2\mu} [\Psi_{\text{NO}^-} \nabla_r \Psi_{\text{NO}^-}^* - (\nabla_r \Psi_{\text{NO}^-}) \Psi_{\text{NO}^-}^*] \\ &= \frac{\hbar}{\mu} \text{Im}(\Psi_{\text{NO}^-} \nabla_r \Psi_{\text{NO}^-}^*). \end{aligned} \quad (33)$$

The flux is integrated to give the total probability for dissociation,

$$P_{\text{diss,NO}^-}(E) = \int_0^t \int_{Z_{\text{min}}}^{Z_{\text{max}}} \mathbf{F}(Z, t') dZ dt'. \quad (34)$$

The recipe for determining the NO⁻ vibrational distribution utilizes the following equation:

$$\sigma_n = \left| \int_{Z_{\text{min}}}^{Z_{\text{max}}} dZ \int_{r_{\text{min}}}^{r_{\text{max}}} dr L_n^*(r) \Psi_{\text{NO}^-}(Z, r; t) \right|^2, \quad (35)$$

where $L_n(r)$ is the n th Laguerre polynomial.

V. NUMERICAL RESULTS AND DISCUSSION

The theoretical methods described in Sec. IV were utilized to simulate the scattering of NO⁺ ($v = 0, 2, 4, 6$) on GaAs(110). The collision energy and initial vibrational states were selected to mimic the experimental conditions.² Each series of quantum trajectories sampled sixteen initial molecular orientations ranging from 0° to 90° relative to the surface normal. The orientations from 90° to 180° have been reported to give a similar set of results classically¹⁶ and thus were not sampled in this calculation.

A. Vibrational enhancement in O⁻ formation

The experimentally observed enhancement in O⁻ emergence with increasing NO⁺ vibrational quanta was simulated for a collision energy of 45 eV. Figure 5 illustrates the computational predictions from the model as well as the experimental results. Figures 5(a) and 5(b) exhibit a remarkably similar enhancement in the O⁻ yield with v^+ . It was discussed in Ref. 2 that the experimental relative yield is associated with collecting ~5% of the scattered products, whereas the model's absolute yield counts all products, regardless of scattering angle. Taking this factor of 20 into consideration, the theoretical predictions are in quantitative agreement with the experimental data; this transpired without any adjustments of the various parameters used in the model.

As a gauge for comparison, quantum trajectories were run under the conditions ($E_{\text{trans}} = 45.0 \text{ eV}$, $v = 0$), ($E_{\text{trans}} = 45.0 \text{ eV}$, $v = 6$), and ($E_{\text{trans}} = 46.7 \text{ eV}$, $v = 0$). The latter two sets correspond to the same total energy, albeit allocated differently between translational and vibrational components. The model demonstrates a 5% enhancement in the O⁻ yield with the addition of 1.7 eV of translational energy, in contrast to a 130% enhancement with the identical amount of energy added to vibration instead. The order of magnitude greater efficacy for vibrational energy relative to translational energy appears in both the experimental and simulated O⁻ product yield (see Fig. 1).

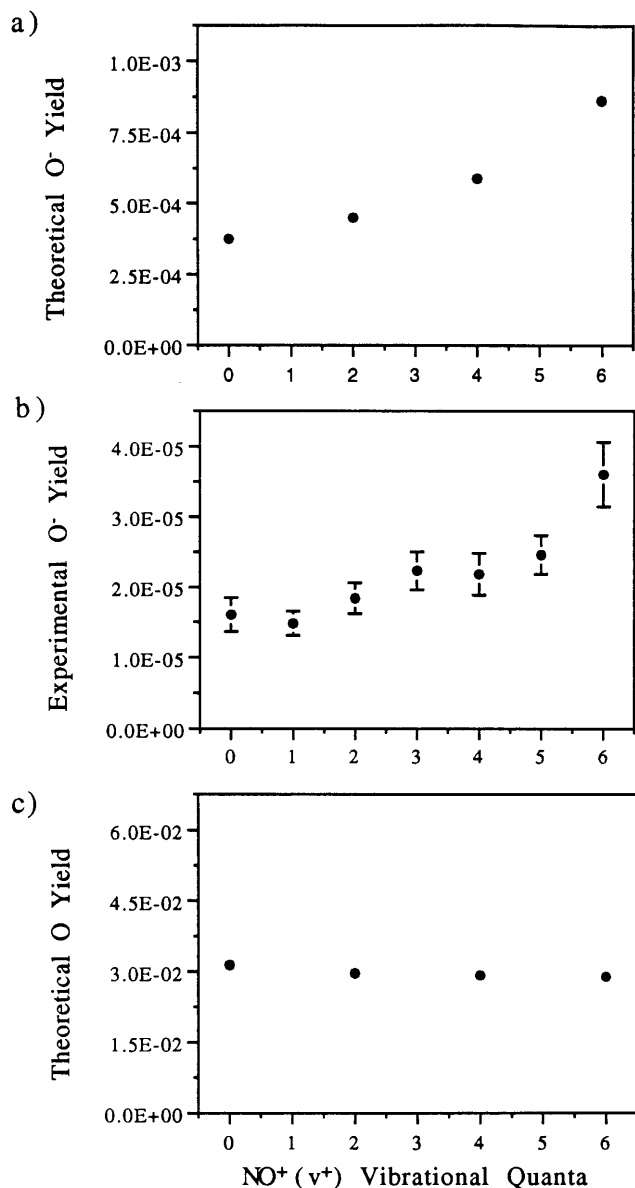


FIG. 5. The (a) theoretical absolute yield of O⁻, (b) the experimental relative yield of O⁻, and (c) the theoretical absolute yield of O vs the number of vibrational quanta in NO⁺(v⁺), incident at 45 eV collision energy.

In a previous study,¹⁶ classical mechanical calculations performed on this system were unable to reproduce the observed vibrational effect. However, the classical trajectories excluded electron transfer and described only Newtonian motion on the neutral PES. Within the present quantum mechanical model, Fig. 5(c) illustrates that fragmentation to form neutral O exhibits a slightly negative vibrational effect. Hence, neither CID alone nor CID following neutralization can adequately explain the observed vibrational enhancement. Clearly, the electron attachment process plays a vital role in the overall vibrational dynamics of O⁻ formation.²

As discussed in the context of the CTC study,¹⁶ rotational excitation upon collision is essential to the CID process. Rotational torques are introduced when a molecule impacts the surface with its internuclear axis directed away from both the surface normal and the surface plane. Figure 6(a) illustrates the differential O⁻ yield as a function of the

incident NO⁺ molecular orientation. In this paper, the term “differential” yield, refers to the fraction of incident ions which appear as products per solid angle element of initial molecular orientations. The corresponding total yield is the integrated differential yield using spherical coordinates. In agreement with the classical trajectory results, Fig. 6(a) suggests that incident molecular orientations near 30° result in the largest O⁻ yield.¹⁶ Comparing the differential O⁻ yield curves for NO⁺(v=0) and NO⁺(v=6), it is evident that the vibrational enhancement in O⁻ production occurs to a similar extent across all initial molecular orientations. Figure 6(b) shows the corresponding differential O yield as a function of the incident NO⁺ molecular orientation. Although the shape of the curves in Figs. 6(a) and 6(b) are similar, the strong vibrational enhancement illustrated in Fig. 6(a) is conspicuously absent in Fig. 6(b). In fact, for initial molecular orientation near 30° the O yield appears to decrease slightly with increasing NO⁺ vibrational quanta.

The curves in Fig. 6(a) are characteristic of the orientation dependence to impulsive energy transfer within a CID mechanism. As such, they underscore the vital role of CID to O⁻ formation. Furthermore, the appearance of a vibrational enhancement in exclusively the O⁻ channel indicates the importance of electron attachment to the overall dynamics. With the latter issue in mind, a more detailed investigation into negative ion formation follows.

B. Negative ion production

The calculated negative ion yield includes both O⁻ and NO⁻ products. Figure 6(c) illustrates the differential negative ion yield as a function of the incident NO⁺ molecular orientation. In comparison with O⁻ formation [see Fig. 6(a)], negative ion formation appears less dependent on initial molecular orientation. This arises principally from the strong orientation dependence for energy transfer within CID, in contrast to the less pronounced orientation dependence to electron attachment in the model.

Figure 6(c) also suggests that negative ion production is universally enhanced with increasing vibrational quanta in incident NO⁺(v⁺). This result initially appears to contradict the experiment, where the relative yield of NO⁻(v⁻=0) was found to be independent of v⁺. However it should be borne in mind that although vibrationally excited NO⁻(v⁻) may be formed at the surface, autoionization limits detection to only NO⁻(v⁻=0).² The calculated *ground state* NO⁻(v⁻=0) population is indeed independent of the initial NO⁺(v⁺) quantum state, completely consistent with the experimental results.² As shown in Fig. 7(a), it is only the vibrationally excited NO⁻ which is enhanced for NO⁺(v⁺=6) over NO⁺(v⁺=0).

The higher degree of NO⁻(v⁻) vibrational excitation following collisions of NO⁺(v⁺=6) as compared to NO⁺(v⁺=0) may arise from a few different sources. To estimate the vibrational excitation originating solely from electron transfer, a simple model is introduced. Two “instantaneous” electron transfers to NO⁺ can be modeled by projecting the initial NO⁺ vibrational eigenstate directly onto the NO⁻PES. The resulting NO⁻(v⁻) vibrational distribution is shown in Fig. 7(b). Although the overall probability for

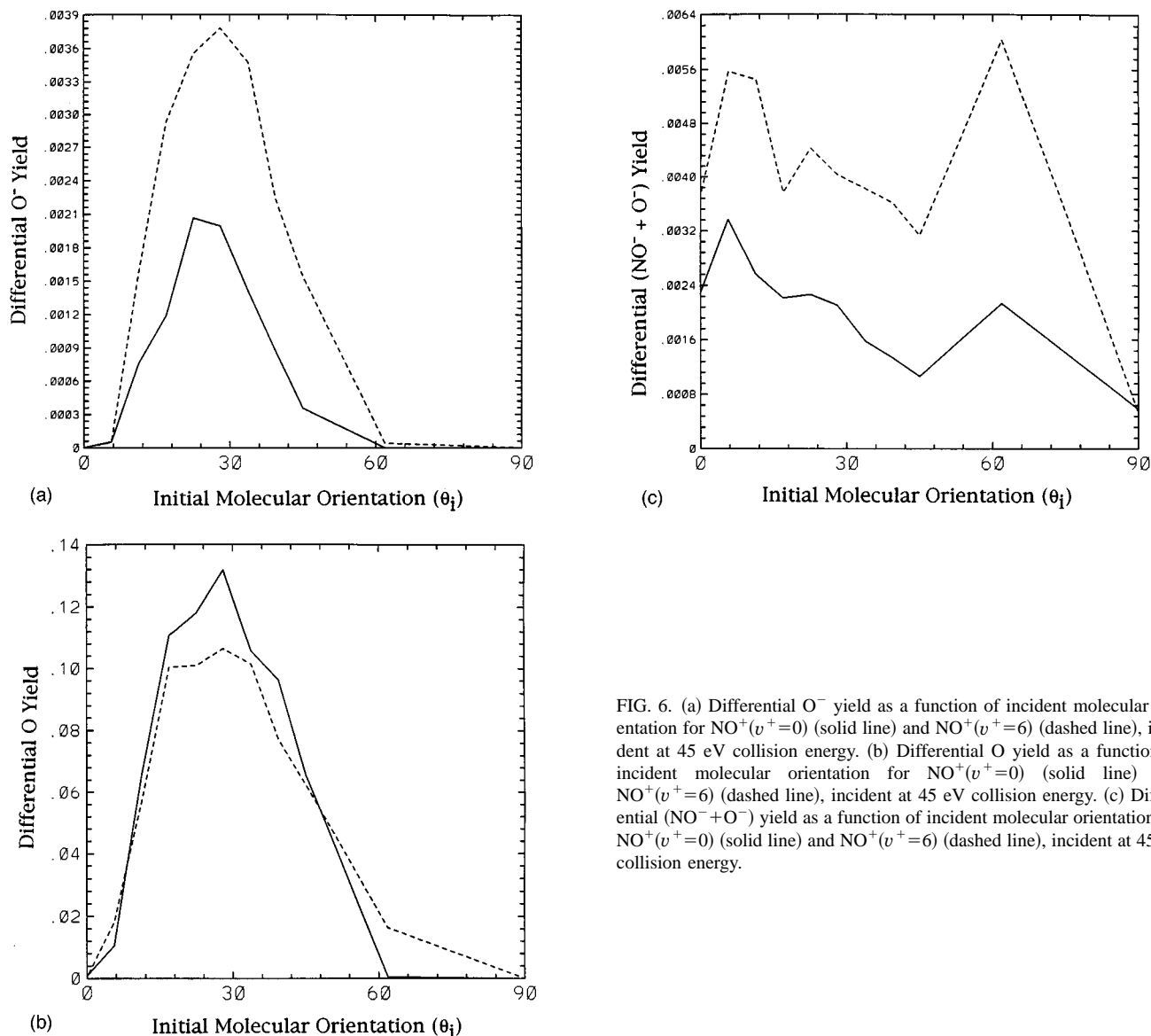


FIG. 6. (a) Differential O⁻ yield as a function of incident molecular orientation for NO⁺($v^+=0$) (solid line) and NO⁺($v^+=6$) (dashed line), incident at 45 eV collision energy. (b) Differential O yield as a function of incident molecular orientation for NO⁺($v^+=0$) (solid line) and NO⁺($v^+=6$) (dashed line), incident at 45 eV collision energy. (c) Differential (NO⁻+O⁻) yield as a function of incident molecular orientation for NO⁺($v^+=0$) (solid line) and NO⁺($v^+=6$) (dashed line), incident at 45 eV collision energy.

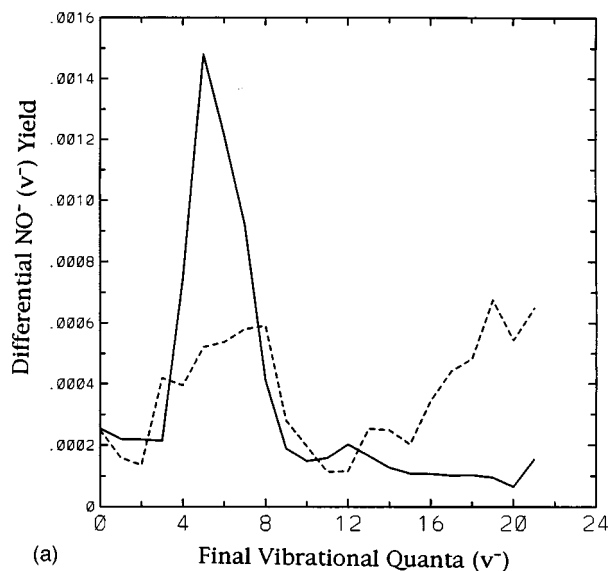
electron attachment appears higher from NO⁺($v^+=6$) than from NO⁺($v^+=0$), the additional population is deposited into low lying vibrational levels. In all cases, the nascent vibrational energy resulting from electron attachment alone is unable to provide the 55 quanta required for dissociation. Allowing the projected wave packet to propagate on the NO PES for a finite amount of time before being projected onto the NO⁻PES, but neglecting CID should not have a major impact on the amount of vibrational excitation formed in NO⁻(v^-). Clearly, the mechanisms for NO⁻ vibrational excitation and O⁻ formation rely not only on electron transfer but on the interplay between impulsive energy transfer and the nuclear dynamics resulting from sequential electronic transitions.

C. Electron transfer dynamics

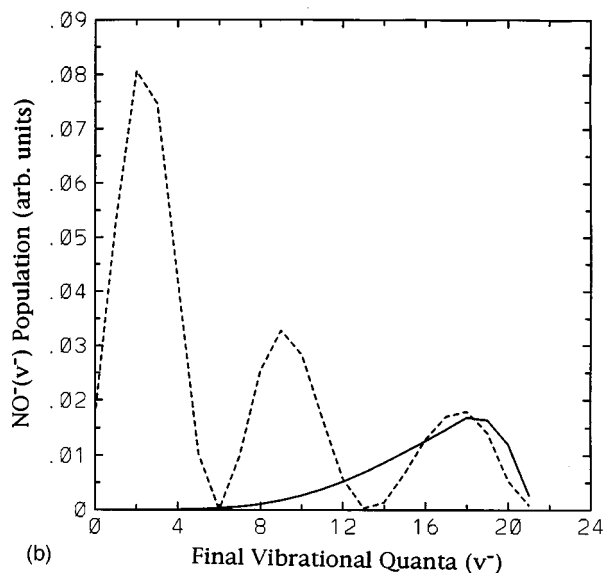
To further visualize the interplay between vibrational motion and electron transfer, Figs. 8(a) and 8(b) display the time-dependence of four dynamical variables during a quan-

tum trajectory. The expectation value of $\langle Z \rangle$ vs time illustrates the diatom scattering from the surface. The time-dependent population on the neutral NO PES demonstrates that neutralization occurs efficiently during the molecule's approach to the surface. Asymptotically, the model predicts that virtually all (98%) of the incident ions are neutralized, in good agreement with experiment.² The energetics of neutralization are most easily seen by comparing the vertical ionization potential of NO with the GaAs density of states [see Fig. 9(a)]. The former quantity is merely the difference between the NO⁺ and NO PES. Resonant neutralization corresponds to the tunneling of an electron from the occupied valence band to the molecular ion. This produces a neutral molecule and a hole in the valence band isoenergetic with the vertical ionization potential. Facile neutralization can be inferred from Fig. 13 which shows that neutralization is resonant throughout the molecule's trajectory.

Resonant electron attachment produces a negative ion and a second hole in the valence band. A similar analysis of



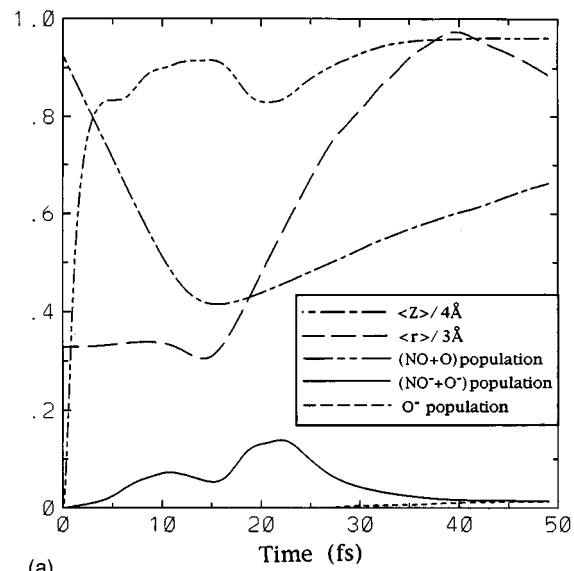
(a)



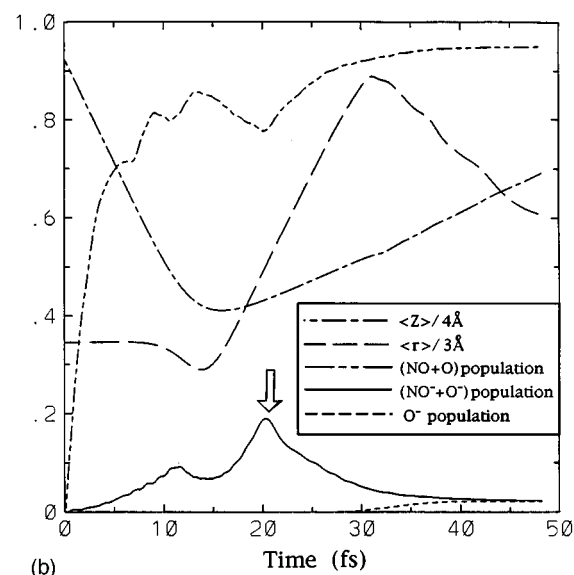
(b)

FIG. 7. (a) The simulated $\text{NO}^-(v^-)$ vibrational distribution resulting from scattering $\text{NO}^+(v^+=0)$ (solid line) and $\text{NO}^+(v^+=6)$ (dashed line) at 45 eV collision energy with an initial molecular orientation of 61.9° . (b) The projected $\text{NO}^-(v^-)$ vibrational distribution for a direct transition from $\text{NO}^+(v^+=0)$ (solid curve) and $\text{NO}^+(v^+=6)$ (dashed curve).

the electron transfer energetics can be applied to negative ion formation. Figure 9(b) illustrates the vertical electron affinity of NO as a function of Z and r . An isolated NO ($v=0$) molecule has a 0.05 eV adiabatic electron affinity. The diatom's vertical electron affinity increases to 2.0 eV as the internuclear distance expands from the equilibrium bond length to 1.7 Å.¹⁵ Moreover, as NO approaches the surface, the electron affinity also increases, because NO^- is stabilized by its image charge in the dielectric. The affinity level is most closely resonant with the GaAs occupied density of states when the molecule is vibrationally stretched and proximate to the surface. Figures 8(a) and 8(b) track the time-dependent population on the negative ion PES. The electron attachment rate increases as $\langle Z \rangle$ decreases, because the coupling strength grows exponentially with decreasing Z . Nevertheless, before the classical turning point, the negative ion



(a)



(b)

FIG. 8. (a) Quantum trajectories of $\text{NO}^+(v^+=0)$ incident at 45 eV collision energy with an initial molecular orientation of 22.5° . (b) Quantum trajectories of $\text{NO}^+(v^+=6)$ incident at 45 eV collision energy with an initial molecular orientation of 22.5° . The arrow indicates the second surge of electron transfer (see text).

population crests at 12 fs. The falloff in electron attachment is concurrent with a compression of $\langle r \rangle$ and correspondingly an unfavorable negative electron affinity. However, a second surge of electron transfer commences at 16 fs, when $\langle r \rangle$ begins to rapidly expand while $\langle Z \rangle$ is still small. Here, the electron affinity reaches a maximum, and electron attachment becomes nearly resonant. After 20 fs, the negative ion population diminishes again as Z increases, and the coupling vanishes. The O^- yield is defined as that portion of the negative ion wavepacket which extends beyond $r=3$ Å. The calculated O^- yield rises after 28 fs and plateaus near 40 fs.

Figures 8(a) and 8(b) compare the quantum trajectories arising from $\text{NO}^+(v^+=0)$ and $\text{NO}^+(v^+=6)$ evaluated for a common incident molecular orientation of 22.5° . Although the wave packet dynamics are quite complex, some differences can be noted in these two figures. Neutralization oc-

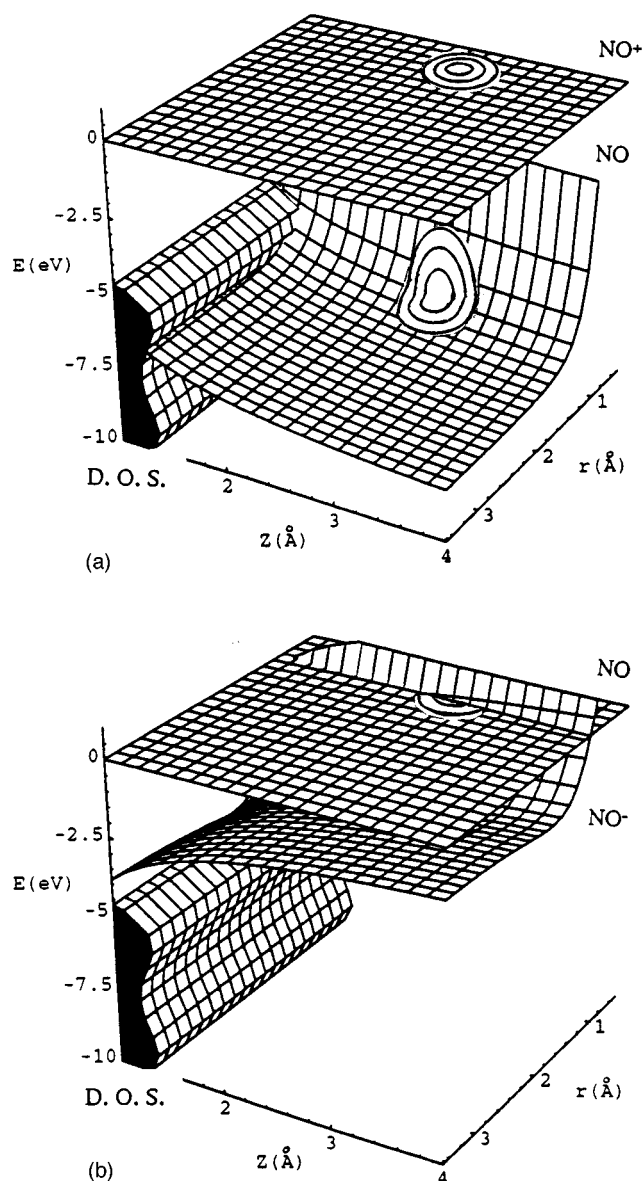


FIG. 9. (a) Resonant neutralization, where the GaAs valence band is compared to the vertical ionization potential of NO as a function of Z and r . The circular contours illustrate an incident NO^+ wave packet being projected onto the NO electronic surface. The vertical ionization potential is resonant with the occupied density of states (D.O.S.) for GaAs. (b) Resonant electron attachment, where the GaAs valence band is compared to the vertical electron affinity of NO as a function of Z and r . The circular contours represent a neutralized NO wave packet with an electron affinity close to zero. Negative ion formation occurs when the wavepacket propagates towards large r and small Z , where the electron affinity comes into resonance with the occupied density of states (D.O.S.) for GaAs.

occurs more slowly from $\text{NO}^+(v^+=6)$ than from $\text{NO}^+(v^+=0)$. This difference in the neutralization rate is further revealed in Figs. 10(a) and 10(b) which show the respective wave packets formed on the neutral ($\text{NO}+h_i^+$) PES. As illustrated in Fig. 9(a), the entire $\text{NO}^+(v^+=0)$ wave function is resonant with the occupied density of states; however, the small r portion of the $\text{NO}^+(v^+=6)$ wave function is less resonant with the GaAs valence band. Hence, the amplitude in Fig. 10(b) is attenuated at short r , and the neutralization rate from $\text{NO}^+(v^+=6)$ is less than that from $\text{NO}^+(v^+=0)$.

At 10 fs (approximately half of a vibrational period) on the ($\text{NO}+h_i^+$) PES, the small r portion of the wave packet propagates to large r , and the large r portion of the wave packet moves to small r . Figure 10(c) shows that the $\text{NO}^+(v^+=0)$ wave packet born on the repulsive wall of the ($\text{NO}+h_i^+$) PES corresponds to a vibrationally expanded molecule after 10 fs. Similarly, the nodal structure of the wave packet originating from $\text{NO}^+(v^+=6)$ appears to have inverted between Figs. 10(b) and 10(d). At approximately 10–15 fs, the NO molecule becomes compressed upon impact with the surface. A comparison of Figs. 8(a) and 8(b) reveals that the $\text{NO}^+(v^+=6)$ trajectory achieves a greater degree of vibrational compression at the classical turning point and subsequently undergoes a more rapid vibrational expansion. This result is consistent with classical trajectory calculations which demonstrate that molecules in a compressed phase of vibration upon surface impact receive a larger vibrational excitation than do molecules that are vibrationally expanded at the moment of impact.¹⁴ Thus, neutralization prepares a coherent v^+ -dependent vibrational wave packet on the ($\text{NO}+h_i^+$) PES which is amplified upon collision with the surface.

A comparison of Figs. 8(a) and 8(b) reveals that at approximately 20 fs $\langle Z \rangle$ is smaller, and $\langle r \rangle$ is larger for the case of $\text{NO}^+(v^+=6)$ compared to $\text{NO}^+(v^+=0)$. Correspondingly, the second surge in electron attachment is more effective for $\text{NO}^+(v^+=6)$. The wave packet's leading edge along the r coordinate undergoes electron attachment most readily, and it is the same portion of the wave front which comprises the O^- product flux. This component of the NO wave packet can be traced back to amplitude which transferred from the NO^+ PES at large r and early time. Figures 10(e) and 10(f) show the wave packet on the ($\text{NO}^-+h_i^++h_1^+$) PES at 24.7 fs, following the quantum scattering of $\text{NO}^+(v^+=0)$ and $\text{NO}^+(v^+=6)$, respectively. The increased amplitude at large r in Fig. 10(f) in contrast to that in Fig. 10(e) testifies to the enhanced O^- yield resulting from the reactive scattering of $\text{NO}^+(v^+=6)$ compared to $\text{NO}^+(v^+=0)$.

The simulation also suggests that back-electron transfer from NO^- to NO is not as severe in the $\text{NO}^+(v^+=6)$ quantum trajectory as in the $\text{NO}^+(v^+=0)$ quantum trajectory. Between 20 and 40 fs in Figs. 8(a) and 8(b), amplitude is coupled from the ($\text{NO}^-+h_i^++h_1^+$) PES back to the ($\text{NO}+h_i^+$) PES. The more rapid expansion along r for the $\text{NO}^+(v^+=6)$ quantum trajectory produces a shorter coupling time and consequently less back-electron transfer than that found in the $\text{NO}^+(v^+=0)$ quantum trajectory.

VI. SUMMARY

A wave packet method with several innovative components has been developed to treat electron and energy transfer for a molecule scattering on a solid surface. Electron transfer transpires through a coupling between the band of substrate electronic states and individual molecular electronic states. Empirical potential energy surfaces are used to describe both the ground and excited state intramolecular forces, as well as the molecule–surface diabatic potentials and nondiabatic couplings. Several additional simplifying as-

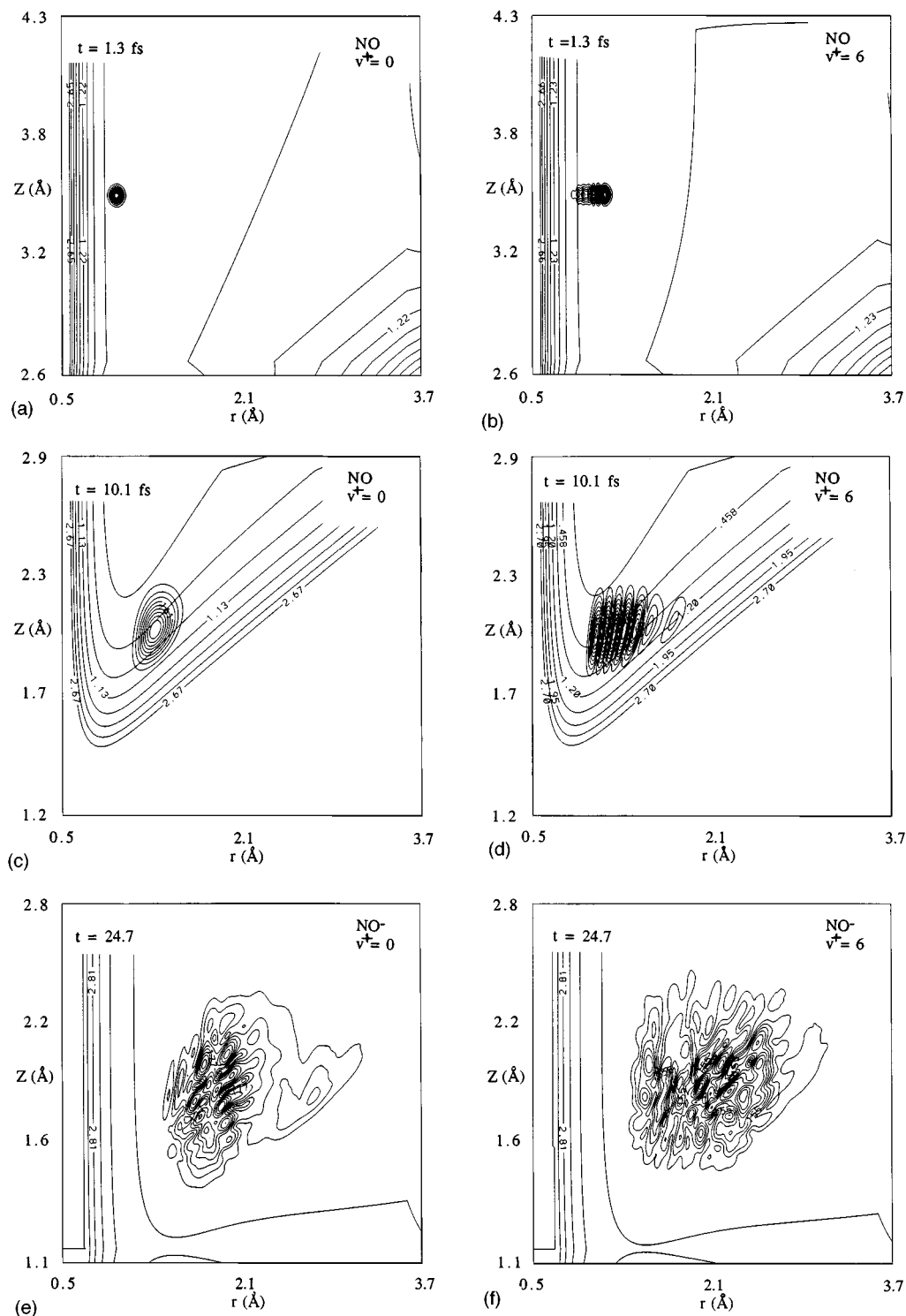


FIG. 10. (a) Absolute value of the wave packet on the $(\text{NO}+h_i^+)$ PES after 1.3 fs. $\text{NO}^+(v^+=0)$ is incident at 45 eV collision energy with an initial molecular orientation of 22.5° . The contour maximum is 1.34; here and below, the contour minimum is 0 and the contour interval is $(\text{max}-\text{min})/10$. All PES contours are in units of eV. (b) The wave packet on the $(\text{NO}+h_i^+)$ PES after 1.3 fs. $\text{NO}^+(v^+=6)$ is incident at 45 eV collision energy with an initial molecular orientation of 22.5° . The contour maximum is 0.691. (c) The wave packet on the $(\text{NO}+h_i^+)$ PES after 10.1 fs. $\text{NO}^+(v^+=0)$ is incident at 45 eV collision energy with an initial molecular orientation of 22.5° . For clarity, the figure portrays only the amplitude transferred to the $(\text{NO}+h_i^+)$ PES in the first 1 fs. The contour maximum is 0.403. (d) The wave packet on the $(\text{NO}+h_i^+)$ PES after 10.1 fs. $\text{NO}^+(v^+=6)$ is incident at 45 eV collision energy with an initial molecular orientation of 22.5° . For clarity, the figure portrays only the amplitude transferred to the $(\text{NO}+h_i^+)$ PES in the first 1 fs. The contour maximum is 0.245. (e) The wave packet on the $(\text{NO}+h_i^++h_i^+)$ PES after 24.7 fs. $\text{NO}^+(v^+=0)$ is incident at 45 eV collision energy with an initial molecular orientation of 22.5° . The contour maximum is 0.387. The interval for the PES contours is 0.379 eV. (f) The wavepacket on the $(\text{NO}+h_i^++h_i^+)$ PES after 24.7 fs. $\text{NO}^+(v^+=6)$ is incident at 45 eV collision energy with an initial molecular orientation of 22.5° . The contour maximum is 0.442. The interval for the PES contours is 0.381 eV.

assumptions were made. The nondiabatic couplings were taken to be independent of N–O molecular orientation and bond length. Moreover, interaction with only a single surface atom was included explicitly. A hyperthermal collision involves predominantly a short range repulsive interaction between the molecule and the single closest surface atom. Although an incident molecule may undergo multiple collisions with the corrugated GaAs(110) surface, it is believed that the dissociation dynamics is mediated primarily by the first collision. Finally, a mixed classical-quantum TDSCF approach was used to calculate the dynamics: the translational and vibrational motion of NO, as well as the electron transfer, were treated quantum mechanically using time-dependent wave packet methods, while the rotational motion and the surface atom motion were treated classically.

The method was used to explore the effect of initial vibrational state-selection for $\text{NO}^+(v^+=0-6)$ scattering on the GaAs(110) surface. The effect of reactant translational and vibrational energies on the yield of O^- and NO^- products is in quantitative agreement with experiment. With regards to negative ion production, the calculation suggests the following scenario for the dynamics along the vibrational coordinate (r). Neutralization occurs readily along the inbound trajectory. The portion of the wavepacket born early on the attractive (large r) portion of the neutral PES expands most rapidly after surface impact. As the neutral diatom expands, electron attachment proceeds preferentially to that portion of the wavepacket that corresponds to trajectories which achieve the largest value of r while at small Z . These same trajectories have reduced probability for back-electron transfer to form the neutral, because they leave the region of maximum interaction quickly. The quantum simulation successfully reproduces the experimentally observed enhancement in the O^- yield with increasing $\text{NO}^+(v^+)$ vibrational quanta; the enhancement can be traced to the increased amplitude, located at the outer turning point of the initial NO^+ vibration, accompanying higher v^+ levels. In agreement with experiment, the calculations predict that the $\text{NO}^-(v^-=0)$ yield is independent of the initial $\text{NO}^+(v^+)$ vibrational quanta.

ACKNOWLEDGMENTS

J.Q. wishes to thank J. S. Martin and J. R. Morris for helpful discussions, and R. Kosloff for insightful discussions. D.C.J. acknowledges the Alfred P. Sloan Foundation for a

Research Fellowship and the National Science Foundation (CHE93-1155). D.J.T. acknowledges the Alfred P. Sloan Foundation for support and the National Science Foundation (CHE94-8432).

- ¹D. C. Jacobs, *J. Phys. Condensed Matter* **7**, 1023 (1995).
- ²J. S. Martin, J. N. Greeley, J. R. Morris, and D. C. Jacobs, *J. Chem. Phys.* **97**, 9476 (1992); J. S. Martin, J. N. Greeley, J. R. Morris, B. T. Feranchak, and D. C. Jacobs, *ibid.* **100**, 6791 (1994).
- ³C. Lim, J. C. Tully, A. Amirav, P. Trevor, and M. J. Cardillo, *J. Chem. Phys.* **87**, 1808 (1987); C. W. Muhlhausen, L. R. Williams, and J. C. Tully, *ibid.* **83**, 2594 (1985); G. O. Sitz, A. C. Kummel, R. N. Zare, and J. C. Tully, *ibid.* **91**, 2572 (1989).
- ⁴E. J. J. Kirchner, E. J. Baerends, U. van Slooten, and A. W. Kleyn, *J. Chem. Phys.* **97**, 3821 (1992).
- ⁵S. Kumar and B. Jackson, *J. Chem. Phys.* **100**, 5956 (1994).
- ⁶M. Hand and S. Holloway, *Surf. Sci.* **211/212**, 940 (1980); D. Halstead and S. Holloway, *J. Chem. Phys.* **88**, 7197 (1988); *ibid.* **93**, 9145 (1990).
- ⁷J. W. Gadzuk, *Annu. Rev. Phys. Chem.* **39**, 395 (1988); R. Kosloff and O. Citri, *Faraday Discuss.* **96**, 1 (1993).
- ⁸P. Saalfrank, R. Baer, and R. Kosloff, *Chem. Phys. Lett.* **230**, 463 (1994); S. M. Harris, S. Holloway, and G. R. Darling, *J. Chem. Phys.* **102**, 8235 (1995).
- ⁹D. M. Newns, K. Makoshi, R. Brako, and J. N. M. van Wunnik, *Phys. Scr.* **T6**, 5 (1983).
- ¹⁰P. W. Anderson, *Phys. Rev.* **124**, 41 (1961).
- ¹¹R. Brako and D. M. Newns, *Rep. Prog. Phys.* **52**, 655 (1989).
- ¹²J. Los and J. J. C. Geerlings, *Phys. Rep.* **190**, 133 (1990).
- ¹³A. Bringer, J. Harris, and J. W. Gadzuk, *J. Phys. Condensed Matter* **5**, 5141 (1993); J. W. Gadzuk, L. J. Richter, S. A. Buntin, D. S. King, and R. R. Cavanagh, *Surf. Sci.* **235**, 317 (1990).
- ¹⁴J. S. Martin, B. T. Feranchak, J. R. Morris, J. N. Greeley, and D. C. Jacobs, *J. Chem. Phys.* (in press).
- ¹⁵J. R. Morris, J. S. Martin, J. N. Greeley, and D. C. Jacobs, *Surf. Sci.* **330**, 323 (1995).
- ¹⁶J. N. Greeley, J. S. Martin, J. R. Morris, and D. C. Jacobs, *J. Chem. Phys.* **102**, 4996 (1995).
- ¹⁷R. B. Gerber and A. Amirav, *J. Phys. Chem.* **90**, 4483 (1986).
- ¹⁸P. J. van den Hoek and A. W. Kleyn, *J. Chem. Phys.* **91**, 4318 (1989).
- ¹⁹J. C. Tully and R. K. Preston, *J. Chem. Phys.* **55**, 562 (1971); J. C. Tully, *ibid.* **93**, 1061 (1990).
- ²⁰U. Fano, *Rev. Mod. Phys.* **29**, 74 (1957).
- ²¹A. W. Kleyn, J. Los, and E. A. Gislason, *Phys. Rep.* **90**, 1 (1982).
- ²²E. Bauer, E. R. Fisher, and F. R. Gilmore, *J. Chem. Phys.* **51**, 4173 (1969).
- ²³J. W. Gadzuk, *Comments At. Mol. Phys.* **16**, 219 (1985).
- ²⁴S. Holloway and J. W. Gadzuk, *J. Chem. Phys.* **82**, 5203 (1985).
- ²⁵P. Nordlander and J. C. Tully, *Phys. Rev. B* **42**, 5564 (1990); P. Nordlander, *ibid.* **46**, 2584 (1992).
- ²⁶R. H. Bisseling, R. Kosloff, and R. B. Gerber, *J. Chem. Phys.* **87**, 2760 (1987); J. Campos-Martinez, J. R. Waldeck, and R. D. Coalson, *ibid.* **96**, 3613 (1992); N. Makri, *Chem. Phys. Lett.* **169**, 541 (1990).
- ²⁷R. B. Gerber, R. Kosloff, and M. Berman, *Comp. Phys. Rep.* **5**, 59 (1986).
- ²⁸C. Leforestier, R. H. Bisseling, C. Cerjan, M. D. Feit, R. Friesner, A. Guldberg, A. Hammerich, G. Jolicard, W. Karrlein, H. D. Meyer, N. Lipkin, O. Roncero, and R. Kosloff, *J. Chem. Phys.* **94**, 59 (1991).